Solar Phys (2017) 292:80
DOI 10.1007/s11207-017-1099-y

A Study of the Earth-Affecting CMEs of Solar Cycle 24

Phillip Hess[1] · **Jie Zhang**[2]

Received: 15 October 2016 / Accepted: 21 April 2017

Abstract Using *in situ* observations from the *Advanced Composition Explorer* (ACE), we have identified 70 Earth-affecting interplanetary coronal mass ejections (ICMEs) in Solar Cycle 24. Because of the unprecedented extent of heliospheric observations in Cycle 24 that has been achieved thanks to the *Sun Earth Connection Coronal and Heliospheric Investigation* (SECCHI) instruments onboard the *Solar Terrestrial Relations Observatory* (STEREO), we observe these events throughout the heliosphere from the Sun to the Earth, and we can relate these *in situ* signatures to remote sensing data. This allows us to completely track the event back to the source of the eruption in the low corona. We present a summary of the Earth-affecting CMEs in Solar Cycle 24 and a statistical study of the properties of these events including the source region. We examine the characteristics of CMEs that are more likely to be strongly geoeffective and examine the effect of the flare strength on *in situ* properties. We find that Earth-affecting CMEs in the first half of Cycle 24 are more likely to come from the northern hemisphere, but after April 2012, this reverses, and these events are more likely to originate in the southern hemisphere, following the observed magnetic asymmetry in the two hemispheres. We also find that as in past solar cycles, CMEs from the western hemisphere are more likely to reach Earth. We find that Cycle 24 lacks in events driving extreme geomagnetic storms compared to past solar cycles.

Keywords Space weather · Coronal mass ejection · Solar wind · Heliosphere

Earth-affecting Solar Transients
Guest Editors: Jie Zhang, Xochitl Blanco-Cano, Nariaki Nitta, and Nandita Srivastava

✉ P. Hess
phillip.hess.ctr@nrl.navy.mil

✉ J. Zhang
jzhang7@gmu.edu

[1] NRC Research Associate, U.S. Naval Research Laboratory, Washington D.C., USA

[2] Department of Physics and Astronomy, George Mason University, Fairfax, VA, USA

Published online: 12 June 2017

1. Introduction

Coronal mass ejections (CMEs) are among the most powerful forms of solar activity. These eruptions of magnetized plasma from the corona propagate through and interact with the solar wind. CMEs can cause numerous harmful effects at Earth, including the damage of satellites and power grids and the disruption of radio communications and air travel (Pulkkinen, 2007). Generally, the Earth will be protected from the solar wind by the magnetosphere that is formed from its internal magnetic field. The way for the solar wind to penetrate the magnetosphere is the presence of a strong southward interplanetary magnetic field, which will cause reconnection along the magnetopause. A CME, because of its strong internal magnetic field, is one of the most common structures capable of causing this reconnection and space weather effects at Earth.

Of all datasets in which CME and CME-related phenomena have been observed, *in situ* observations are among the most well studied. Taken from a spacecraft measuring the solar wind magnetic field and plasma parameters, such as density and velocity, at one particular point in space, *in situ* measurements provide a time series of the solar wind as it passes through the spacecraft. CME signatures have long been seen in these data sets, and have been called interplanetary coronal mass ejections (ICMEs), to make clear the connection between these structures and those observed closer to the Sun (Richardson and Cane, 2004).

The longest continuous observational data set of CMEs near the Sun has been provided by the *Large Angle Spectroscopic Coronagraph* (LASCO: Brueckner *et al.*, 1995) onboard the *Solar and Heliospheric Observatory* (SOHO), launched in 1995. These coronagraphs have continued to provide white-light imaging of the solar corona to a distance of approximately $\sim 30\ R_{\odot}$. LASCO has observed thousands of CMEs close to the Sun, and has provided a way to link the signatures detected *in situ* back to the Sun. However, the limited LASCO field of view left more than 80% of an astronomical unit (AU) gap between the edge of the coronagraph observations and the detection of the CME *in situ*. This large gap in spatial data coverage means there can be large discrepancies in the identification of an observed eruption in a coronagraph and the event detected *in situ*.

The launch of the *Solar Terrestrial Relations Observatory* (STEREO) in 2006 offered unprecedented observations of CMEs in the heliosphere. The STEREO mission consisted of two spacecraft, one traveling ahead (A) of the Earth and the other behind (B). Combined with SOHO observations from the L1 point, three separate and distinct observing locations of the heliosphere have provided a better ability to observe CMEs in Solar Cycle 24. Additionally, STEREO contains the *Sun Earth Connections Coronal and Heliospheric Investigation* (SECCHI: Howard *et al.* 2008), a series of instruments that present continuous spatial coverage of heliospheric observations from the low corona to 1 AU. Using SOHO alone, remote-sensing observations of CMEs were limited to the low corona. Combining the observations from the different SECCHI instruments, CMEs using STEREO can be tracked completely from the Sun to the Earth.

Compared to the data available in Solar Cycle 23, SECCHI allows for a more complete observational ability to track a CME from the corona as it evolves in the heliosphere beyond 1 AU. In the past, researchers were forced to infer the connectivity between the corona and the Earth and to make assumptions about the nature of CME propagation in the heliosphere (Gopalswamy *et al.*, 2001; Wang *et al.*, 2002; Zhang *et al.*, 2003, 2007), but we can now be more accurate and confident in relating white-light signatures to their *in situ* counterparts in Cycle 24 (Rouillard, 2011; Shen *et al.*, 2014).

This observational advantage is not present throughout the entire Cycle 24, however. When the STEREO spacecraft began to pass behind the Sun, no data were received, limiting

the observations of events after September 2014. STEREO-A began transmitting observations again in December 2015, while STEREO-B is still not providing data. In the interim, the observations of the heliosphere are similar to what was available in Cycle 23.

As part of the International Study of Earth-affecting Solar Transients (ISEST), a list of Earth-affecting coronal mass ejections was generated that covers the STEREO era. There can be a high degree of ambiguity in ICME signatures, so that different observers may have different interpretations of these events. By comparing the ICME signatures with the white-light SECCHI data, we can more reliably determine what is truly a CME-related structure in *in situ* data, and understand exactly where this structure came from near the Sun.

We consider any event that generates an identifiable ICME signature at Earth to be Earth-affecting, regardless of whether the event actually triggered a geomagnetic storm. We focus only on events that are detected at Earth because these events possess a number of observational advantages. The heliospheric imagers onboard STEREO are being consistently pointed to provide maximum coverage of the Sun–Earth line. The better a CME is aligned toward Earth, the better it will be observed. For example, the 23 July 2012 Carrington Event (Temmer and Nitta, 2015) was an impulsive CME that has been well observed in coronagraphs and was well aligned with STEREO-A on the far side of the Sun, providing a strong *in situ* signature at STEREO-A. However, the orientation of the heliospheric imagers prevented them from clearly observing this CME beyond the COR2 field of view. Furthermore, Earth-directed CMEs can also be observed in the corona in EUV wavelengths and magnetogram observations.

The EUV observations before 2010 come from the SOHO/*Extreme-Ultraviolet Imaging Telescope* (EIT: Delaboudiniere *et al.*, 1995), which observed the corona in four different wavelengths. After the launch of the *Solar Dynamics Observatory* (SDO), the extreme ultraviolet observations came from the *Atmospheric Imaging Assembly* (AIA: Lemen *et al.* 2012) that provides observations at a greatly improved temporal and spatial cadence in ten different wavelengths. The improvement of AIA allows for improved observations of even the weakest of events.

Section 2 of this article explains our method for selecting events. Section 3 presents the actual events with basic information on each of them. An analysis of the event data, including *in situ* parameters and relationships with solar data, is presented in Section 4. This section also includes a comparison of these data with other CME studies from Cycles 23 and 24. Section 5 summarizes the events and presents a brief discussion.

2. Method

Earth-affecting ICMEs were identified using *in situ* data from the *Advanced Composition Explorer* (ACE: Stone *et al.*, 1998), a satellite at the L1 point near the Earth that is capable of observing both magnetic fields and plasma properties in the solar wind. The classic signature of an ICME is a magnetic cloud (Burlaga, 1988), which consists of a depressed density and temperature and an enhanced magnetic field strength with a gradual transition between positive and negative in at least one component direction, indicating the rotation of the flux rope magnetic field around a central axis. The dropping of the density and temperature inside the flux rope lead to a much lower plasma pressure in the ICME than in the ambient solar wind. This, combined with the increased magnetic pressure, causes the plasma β, the ratio between kinetic and magnetic pressure, to be lower inside the flux rope than in the solar wind.

Additionally, interplanetary shocks are often seen ahead of these signatures, indicated by sharp, nearly instantaneous increases in magnetic field, temperature, and density (Jackson, 1986). The sheath region of compressed solar wind plasma between the flux rope and the shock has been shown to contribute almost 30% of the energy of a geomagnetic storm (Zhang, Poomvises, and Richardson, 2008).

In practice, however, very few ICMEs present ideal signatures. Interacting CMEs can lead to complex *in situ* signatures that are more difficult to interpret, and may be more likely to lead to extreme space weather (Burlaga, Plunkett, and St. Cyr, 2002; Wang *et al.*, 2003a,b; Wang, Ye, and Wang, 2003; Möstl *et al.*, 2012; Lugaz *et al.*, 2015). CMEs that are not pointed directly at Earth can also lead to *in situ* data that are not observed as a perfect magnetic cloud because the leg of the CME impacts the Earth (Zhang, Hess, and Poomvises, 2013). There are also other transients that can be detected *in situ* and lead to geomagnetic storms, such as corotating interacting regions (CIRs) (Richardson *et al.*, 2006).

To determine a list of ICME events, we specifically searched for periods of enhanced magnetic field (peak > 10 nT), with depressed proton density (< 4 cm^{-3}) and temperature ($T_{\rm ion}/T_{\rm exp} < 1.5$, where $T_{\rm ion}$ is the measured ion temperature and $T_{\rm exp}$ is the expected temperature based on particle velocity) (Richardson and Cane, 1995). These periods are determined through an automated detection algorithm. For any period that displayed at least two of these three signatures, a list of potential events was compiled. The *in situ* signatures were then manually inspected to determine if the event was an ICME, CIR, or other false event.

This list provided the ICMEs observed at the Earth in Cycle 24. To determine the boundaries of the passing ICME, we specifically focus on periods in the solar wind where the plasma $\beta \ll 1$. This could bias our results toward events with stronger magnetic fields, so that our list may exclude some ICMEs with a weaker magnetic field at Earth. It will help us identify the highest potential for geoeffectiveness based on magnetic field strength (with the actual geoeffectiveness determined largely by the magnetic field orientation), however, and provide a consistent means of identifying the ambiguous trailing boundary of the flux rope.

After finding the *in situ* events, the signatures detected at ACE were linked to an eruption from the corona. This was done with SECCHI data, allowing us to trace each event backward from the Earth to observe the full evolution of the CME and verify the solar connection and its heliospheric signal. A detailed example of this full heliospheric tracking as well as the relationship between white-light structures and *in situ* signatures for the 12 – 14 July 2012 CME is presented in Hess and Zhang (2014), including the use of a graduated cylindrical shell model (GCS: Thernisien, Howard, and Vourlidas 2006), using the multiple viewpoints of STEREO and SOHO to reconstruct the three-dimensional geometry of the CME.

By following each event back to the corona, we can also identify the flare or prominence associated to the event and observe the photospheric magnetic field configurations that lead to the eruptions. Knowing the time of CME onset and the time of the arrival at Earth, it also allows us to calculate an average transit velocity for the CME from the Sun to the Earth. The full list, as well as data and discussion pages for the events, can be found at the *ISEST* Wiki.[1]

[1] http://solar.gmu.edu/heliophysics.

3. Detected Events

Between 2007 and 2015, we have a total of 70 ICMEs from ACE observations. These events cover a range of different signatures, including standard magnetic clouds, shocks and sheaths, more complex events of multiple interacting CMEs and/or CIRs, and more ambiguous events that may only contain some with the ICME signatures for which we look. There are also three events that do not show an identifiable CME, but appear to be CME-driven shocks that have reached Earth.

The ICMEs can be difficult to link to white-light observations. An event that presents clear *in situ* signatures is more likely to be well linked with a bright, Earth-directed CME that is well observed through the entire SECCHI field of view. A weaker ICME is likely indicative of a less powerful CME or one of which only the flank of the CME passes through Earth. The lower quality heliospheric observations of these events will make it more difficult to determine whether the detected disturbances at Earth are truly related to the observed coronal eruption.

The events are summarized in Table 1. The data in the table include the arrival times of the ICME signature, which can be either a flux rope structure or the shock in front of the flux rope, as well as the trailing boundary of the event. The trailing boundary is one of the more subjective parameters even for clear events, and the plasma β is used to make the distinction, as most events will show a significant, instantaneous increase between the low flux rope β and that of the solar wind. The CME in LASCO shows the time of the first C2 image in which the CME can be seen, with the exception of the 1 August 2010 event, for which there was a LASCO data gap. The time given for that event is from STEREO/COR2.

We provide a brief classification for the type of event, where "SH" stands for the presence of a shock, "MC" stands for the classic magnetic-cloud-type of event, and "EJ" or ejecta is a more ambiguous ICME signature. "Multiple EJ" means that based on both *in situ* data and remote-sensing observations, this event is a combination of multiple interacting transients. The difference between the detection of the CME in LASCO and the arrival at Earth provides the transit time.

The values in the columns labeled as CDAW width and velocity are based on manual CME tracking in LASCO coronagraphs, taken from the Coordinated Data Analysis Workshops (CDAW) CME catalog[2] (Yashiro *et al.*, 2004). There are five events in our sample that either were not determined to be CMEs in the CDAW catalog or occurred after the most recent update to the catalog in October 2015. The GCS velocities are based on linear fits to height measurements from the GCS model in coronagraph data and were performed for 18 of the events in the table.

The active region number and location are based on NOAA designations, and the flare strength and onset time is taken from GOES data. The active region location is based on the location of the active region at 00:00 UTC on the date in question. Eruptions that occur later in the day could be rotated more than 10° from this location. If the eruption is not associated with an active region, an approximate location was determined for the eruption based on EUV observations, although given the extended spatial range of an eruptive filament, this is an inexact location. It should be noted that even with an ability to track a CME completely back to its source, there is some room for debate about these sources. In addition to the potential errors already discussed, there are also a number of events that are a combination of structures from multiple eruptions. While we attempt to focus on the event that we believe contributes more to the detected ICME signature, this is another potential source of uncertainty.

[2] http://cdaw.gsfc.nasa.gov/CME_list.

Table 1 The catalog of Earth-affecting ICME events from 2007 to 2015. "IP event start" and "IP event end" are the boundaries of the whole ICME. "CME in LASCO" is the time determined from the first arrival of the associated CME in LASCO using the Solar Eruptive Event Detection System (SEEDS). The first appearance of a front in C2 that was connected to the eruption was used to select this time. The active region (AR) and its location are based on NOAA classifications. For events with no active region association, an approximate central eruption location was determined. The flare strength and onset time are taken from GOES data. The Dst peak strength (nT) and time are based on data from the Kyoto Geomagnetic Index Service. "Avg. vel." and $|B|$ are the average internal speed and magnetic field of the transient, as measured by ACE. The quality rating (QR) is an arbitrary determination of the "quality" of the ICME signature, with 1 corresponding to the best events and 3 to the most ambiguous. The asterisk (*) denotes events for which there are not SECCHI observations. All times are in UTC and all velocities in km s^{-1}.

IP event start	IP event end	CME in LASCO	Type	TT	AR	AR loc.	Flare strength	Flare onset	CDAW vel.	CDAW width	GCS vel.	AVG vel.	$\|B\|$	Dst peak	QR
20-Nov-07 0:00	20-Nov-07 11:00	16-Nov-07 8:50	EJ	87	–	N07 W04	–	–	–	–	–	463	17.9	−63	2
17-Dec-08 2:00	18-Dec-08 15:00	12-Dec-08 9:06	EJ	113	–	N36 W10	–	–	203	184	–	324	5.3	–	2
26-Jan-09 5:00	26-Jan-09 15:00	21-Jan-09 21:08	EJ	104	–	S40 W35	–	–	220	73	–	348	9.9	–	3
3-Feb-09 19:00	4-Feb-09 16:00	31-Jan-09 1:54	EJ	89	–	N06 E12	–	–	268	38	–	356	9.9	−48	3
30-Sep-09 6:00	30-Sep-09 18:00	25-Sep-09 8:06	EJ	118	11027	N24 W09	–	–	–	–	–	349	7.8	–	3
29-Oct-09 7:00	29-Oct-09 22:00	23-Oct-09 15:54	EJ	135	–	N09 E15	–	–	197	57	–	371	10.1	–	1
14-Nov-09 3:00	14-Nov-09 23:00	9-Nov-09 20:06	EJ	103	11030	N25 W52	–	–	209	42	–	311	6.4	–	2
1-Jan-10 22:00	3-Jan-10 10:00	27-Dec-09 21:30	EJ	121	11039	S26 E31	B8	27-Dec-09 11:00	90	63	–	283	6.8	–	1
5-Apr-10 8:00	6-Apr-10 15:00	3-Apr-10 10:33	SH+MC	46	11059	S25 W03	B7	3-Apr-10 9:54	668	360	844	630	9.2	−77	1
11-Apr-10 12:00	12-Apr-10 15:00	8-Apr-10 1:54	SH+EJ	82	11060	N24 W00	B5	8-Apr-10 3:00	264	160	516	401	10.3	−66	2
28-May-10 2:00	29-May-10 14:00	23-May-10 18:30	SH+Multiple EJ	104	–	N10 W06	–	–	258	360	487	371	10.8	−91	1
20-Jun-10 20:00	22-Jun-10 14:00	16-Jun-10 15:07	MC	101	–	S24 W24	–	–	236	153	–	370	5.6	–	2
3-Aug-10 18:00	5-Aug-10 8:00	1-Aug-10 3:54	SH+Multiple EJ	62	11092	N20 E36	C3.2	1-Aug-10 8:26	850	360	–	565	7.4	−70	1
28-Dec-10 4:00	28-Dec-10 16:00	23-Dec-10 5:12	EJ	119	–	S15 W18	–	–	286	126	–	345	9.7	−43	3
19-Feb-11 3:00	20-Feb-11 16:00	15-Feb-11 2:36	Multiple EJ	96	11158	S18 W15	X2.2	15-Feb-11 1:56	669	360	788	446	8.2	–	2
29-Mar-11 16:00	1-Apr-11 11:00	25-Mar-11 5:36	Long duration MC	106	11176	S16 E31	C1.4	29-Mar-11 0:38	119	191	197	348	11.4	−41	1

Table 1 (*Continued.*)

IP event start	IP event end	CME in LASCO	Type	TT	AR	AR loc.	Flare strength	Flare onset	CDAW vel.	CDAW width	GCS vel.	AVG vel.	$\|B\|$	Dst peak	QR
17-Jun-11 2:00	17-Jun-11 12:00	14-Jun-11 6:36	SH	67	–	S24 E63	–	–	571	188	–	493	–	–	3
3-Jul-11 3:00	4-Jul-11 15:00	29-Jun-11 0:46	EJ	98	11242	N18 W15	B7	29-Jun-11 0:32	481	122	–	396	7.7	−57	2
5-Aug-11 19:00	6-Aug-11 4:00	4-Aug-11 4:12	SH+CIR+EJ	39	11261	N16 W51	M6.0	4-Aug-11 3:17	610	360	–	533	4.6	−113	2
9-Sep-11 15:00	10-Sep-11 18:00	6-Sep-11 23:05	SH+EJ	64	11283	N14 W18	X2.1	6-Sep-11 22:12	575	360	–	491	11.5	−64	3
17-Sep-11 2:00	18-Sep-11 22:00	14-Sep-11 0:05	SH+EJ	74	11289	N22 W13	–	–	408	242	437	449	8.3	−63	2
22-Oct-11 20:00	23-Oct-11 20:00	16-Oct-11 14:36	EJ	149	–	N06 E12	–	–	246	59	–	308	5	–	3
24-Oct-11 18:00	25-Oct-11 17:00	22-Oct-11 10:36	SH+MC	55	11314	N25 W77	M1.3	22-Oct-11 9:18	1005	360	–	452	20.2	−137	2
1-Nov-11 8:00	3-Nov-11 4:00	27-Oct-11 12:12	SH+EJ	116	–	N18 E06	–	–	570	360	–	373	5.6	−55	3
22-Jan-12 5:00	24-Jan-12 20:00	19-Jan-12 15:12	SH+EJ	62	11402	N28 E14	M2.6	19-Jan-12 13:43	1120	360	–	443	7.7	−73	2
8-Mar-12 11:00	9-Mar-12 15:00	7-Mar-12 0:36	SH+EJ	34	11429	N17 E15	X5.4	7-Mar-12 0:02	2684	360	2846	421	14.9	−133	3
15-Mar-12 13:00	16-Mar-12 10:00	13-Mar-12 17:26	SH+EJ	44	11429	N18 W63	M7.9	13-Mar-12 17:12	1884	360	1529	675	8.1	−74	2
4-Apr-12 22:00	8-Apr-12 3:00	30-Mar-12 14:46	EJ	127	–	N24 W24	–	–	141	44	–	340	7.9	−54	3
23-Apr-12 2:30	24-Apr-12 3:00	19-Apr-12 15:36	EJ+CIR	83	–	S30 E40	–	–	540	142	–	372	28.6	−106	3
16-Jun-12 9:00	16-Jun-12 19:00	14-Jun-12 14:00	SH+MC	43	11504	S17 W00	M1.9	16-Jun-12 12:52	987	360	–	448	13.6	−71	2
8-Jul-12 10:00	10-Jul-12 15:00	5-Jul-12 13:36	EJ	68	11515	S17 W37	M1.0	5-Jul-12 13:05	741	98	–	414	9.9	−65	2
14-Jul-12 17:00	17-Jul-12 5:00	12-Jul-12 16:48	SH+MC	48	11520	S17 W08	X1.4	12-Jul-12 15:36	885	360	1135	482	16.6	−127	1
30-Sep-12 23:00	2-Oct-12 12:00	28-Sep-12 0:00	SH+EJ	71	11577	N09 W24	C3.0	28-Sep-12 0:00	947	360	1133	343	7.9	−119	2
8-Oct-12 5:00	9-Oct-12 19:00	5-Oct-12 3:24	SH+MC	74	11584	S22 W38	–	–	612	284	656	393	14.9	−104	2
31-Oct-12 15:00	3-Nov-12 13:00	27-Oct-12 17:00	SH+MC	94	–	N20 W18	–	–	317	360	373	316	7.3	−60	1
16-Feb-13 11:00	17-Feb-13 15:00	12-Feb-13 23:12	SH+EJ	84	–	S40 W40	–	–	1050	165	–	365	6.8	–	3
17-Mar-13 5:30	19-Mar-13 18:00	15-Mar-13 7:12	SH+MC	46	11692	N09 W05	M1.1	15-Mar-13 5:46	1063	360	857	497	8.4	−132	1
13-Apr-13 22:00	15-Apr-13 20:00	11-Apr-13 7:24	SH+MC	63	11719	N10 W01	M6.5	11-Apr-13 6:55	861	360	794	411	9.8	–	2

Table 1 (*Continued.*)

IP event start	IP event end	CME in LASCO	Type	TT	AR	AR loc.	Flare strength	Flare onset	CDAW vel.	CDAW width	GCS vel.	AVG vel.	$\|B\|$	Dst peak	QR
6-Jun-13 15:00	8-Jun-13 1:00	2-Jun-13 18:24	EJ	93	–	S05 W35	–	–	222	87	–	424	10.2	−73	2
27-Jun-13 13:30	29-Jun-13 12:00	23-Jun-13 22:12	SH+MC	87	11778	S16 E61	M2.9	23-Jun-13 20:48	174	174	–	370	11.2	−97	2
5-Jul-13 18:00	7-Jul-13 18:00	3-Jul-13 7:36	MC	58	11785	S11 E48	M1.5	3-Jul-13 7:00	807	267	–	335	9.7	−79	2
9-Jul-13 20:00	10-Jul-13 20:00	6-Jul-13 19:34	SH+EJ	72	11787	S15 E29	C4.9	6-Jul-13 19:31	380	123	–	428	10.2	−45	2
12-Jul-13 16:30	14-Jul-13 23:00	9-Jul-13 15:12	MC	73	–	N15 E05	–	–	449	360	526	396	12.1	−72	2
2-Oct-13 1:15	3-Oct-13 16:00	29-Sep-13 22:12	SH+EJ	51	–	N10 W30	–	–	1179	360	1060	354	8.1	−67	2
7-Nov-13 0:00	7-Nov-13 18:00	2-Nov-13 4:48	EJ	115	11885	S13 W14	C8.2	2-Nov-13 4:40	828	360	–	359	7.5	−54	3
23-Nov-13 4:00	24-Nov-13 0:00	19-Nov-13 21:15	EJ	79	11893	S13 W79	X1.0	19-Nov-13 10:14	364	106	–	350	7.2	–	3
25-Dec-13 4:00	25-Dec-13 17:00	19-Dec-13 9:36	MC	138	11928	S15 W17	C1.3	18-Dec-13 9:03	230	159	–	292	11	–	2
7-Feb-14 16:00	9-Feb-14 12:00	4-Feb-14 17:48	SH+EJ	70	11967	S13 W24	M1.5	4-Feb-14 15:25	294	127	–	415	7.5	–	3
15-Feb-14 12:00	16-Feb-14 22:00	12-Feb-14 6:36	SH+EJ	77	11974	S12 W11	M3.7	12-Feb-14 3:52	373	360	–	384	12	–	3
27-Feb-14 16:00	28-Feb-14 14:00	25-Feb-14 1:25	SH+EJ	63	11990	S15 E65	X4.9	25-Feb-14 0:39	2147	360	–	436	9.6	−99	3
25-Mar-14 19:30	27-Mar-14 7:00	23-Mar-14 3:48	SH+MC	64	12014	S14 E23	C3.1	23-Mar-14 2:27	820	360	–	395	6.8	–	2
5-Apr-14 10:00	7-Apr-14 14:00	2-Apr-14 14:00	SH+MC	68	12027	N13 E41	M6.6	2-Apr-14 13:18	1471	360	1605	375	11.9	–	2
20-Apr-14 11:00	22-Apr-14 7:00	18-Apr-14 13:25	SH+MC	46	12036	S15 W42	M7.3	18-Apr-14 12:31	1203	360	1145	544	5.6	–	2
29-Apr-14 20:00	1-May-14 0:00	25-Apr-14 0:48	MC	115	12046	S17 W91	X1.3	25-Apr-14 0:17	456	296	–	308	9	−67	2
7-Jun-14 16:00	10-Jun-14 15:00	4-Jun-14 13:48	SH+MC	74	12077	S08 E03	–	–	467	360	–	484	4.4	–	2
19-Aug-14 7:00	21-Aug-14 17:00	15-Aug-14 18:36	Long duration MC	84	–	S17 W10	–	–	342	360	–	353	14.3	–	2
11-Sep-14 23:00	14-Sep-14 3:00	9-Sep-14 0:16	SH+MC	71	12158	N15 E14	M4.6	9-Sep-14 23:12	920	360	–	614	19.9	−75	2
10-Nov-14 1:30*	11-Nov-14 20:00	7-Nov-14 18:08	SH+EJ	55	12205	N15 E33	X1.6	7-Nov-14 16:53	795	293	–	468	8.9	−57	3

Table 1 (*Continued.*)

IP event start	IP event end	CME in LASCO	Type	TT	AR	AR loc.	Flare strength	Flare onset	CDAW vel.	CDAW width	GCS vel.	AVG vel.	$\|B\|$	Dst peak	QR
21-Dec-14 18:30*	23-Dec-14 12:00	17-Dec-14 4:48	SH+EJ	110	12242	S19 W02	M8.7	17-Dec-14 4:25	587	360	–	385	17.6	−51	2
17-Mar-15 4:00*	18-Mar-15 6:00	15-Mar-15 1:48	SH+MC	50	12297	S17 W38	C9.1	15-Mar-15 1:15	719	360	–	562	19.4	−223	2
10-Apr-15 0:00*	11-Apr-15 8:00	4-Apr-15 23:36	EJ	120	–	S30 E20	–	–	825	233	–	393	15.7	−75	3
6-May-15 1:00*	7-May-15 18:00	2-May-15 21:36	SH+MC	75	–	S45 W30	–	–	335	360	–	419	12.3	–	2
21-Jun-15 16:00*	24-Jun-15 12:00	19-Jun-15 6:42	MULTI SH+EJ	57	–	S30 W05	–	–	584	360	–	600	11.3	−204	2
27-Jun-15 3:30*	27-Jun-15 19:00	25-Jun-15 8:36	SH	43	12371	N11 W45	M7.9	25-Jun-15 8:02	1627	360	–	630	–	–	3
13-Jul-15 1:00*	14-Jul-15 14:00	10-Jul-15 2:00	MC	71	–	S45 E15	–	–	348	138	–	500	7.4	−61	1
26-Aug-15 8:00*	28-Aug-15 12:00	22-Aug-15 7:24	EJ	97	12403	S14 E09	M1.2	22-Aug-15 6:39	547	360	–	365	11	−91	3
7-Sep-15 18:00*	9-Sep-15 12:00	4-Sep-15 19:36	MC	70	–	S20 W05	–	–	217	64	–	483	14.1	−98	1
6-Nov-15 17:30*	8-Nov-15 16:00	4-Nov-15 15:12	SH+MC	50	12443	N06 W10	M3.7	4-Nov-15 13:31	–	–	–	505	13.5	−96	2
19-Dec-15 15:30	21-Dec-15 20:00	16-Dec-15 9:36	SH+MC	78	12468	S15 W15	C6.6	16-Dec-15 8:34	–	–	–	391	15.9	−155	1
31-Dec-15 0:00	1-Jan-16 19:00	28-Dec-15 12:12	SH+EJ	60	12473	S22 W18	M1.9	28-Dec-15 11:20	–	–	–	433	11.5	−110	2

The Dst peak is a measure of the enhancement of the Earth's ring current, caused by particle injection from magnetic reconnection with the solar wind. A peak Dst of −100 nT or lower is generally considered to be an intense geomagnetic storm. We consider anything that drops below −40 nT to be a moderate enhancement.

We also include the quality rating, which is a subjective rating of each event. Richardson and Cane (2010) and Zhang *et al.* (2007) used a quality rating based on ICME boundaries and the confidence of solar source identification, respectively. We have used a similar system of quality rating between 1 and 3, but with different criteria.

In our list the quality rating is essentially a confidence rating in our ability to state that the *in situ* signature is CME related and our ability to track the CME back to the Sun. This does not necessarily mean that a quality rating of 1 will be observed as a magnetic cloud, but instead just means that we can definitely say that the event in question is a CME and that we can confidently relate the remote-sensing observations to what is seen *in situ*.

A quality rating of 2 is an event that has some ambiguity, which could be related to a degraded *in situ* signature or the possible presence of another CME or CIR in the observation. A quality rating of 3 pertains to events that still show an obvious signature of some kind at the Earth, but are complex enough that we cannot definitively state that the *in situ* signature is a CME or that the relation between the different observational data sets is accurate. This could be an event that seems to only briefly pass through ACE without clear flux rope parameters, or a CME that has multiple potential candidates that contribute the signature observed by ACE. We do believe that the QR3 events are related to CMEs, but there may be enough ambiguity to make them less useful for a more detailed study.

The quality rating in the catalog was added to emphasize the most well observed events, as these would be the most beneficial for a collaborative study. Because the QR1 events show clear observations in EUV, white light, and *in situ*, we consider these to be the best events for the group to focus on as parts of any campaign study. However, because there are relatively few QR1 events, QR2 events should be good enough to merit consideration for many studies. While there may be some QR3 events that individually warrant a more detailed investigation, on the whole this subset should be considered less reliable for a larger CME study and should be used with caution.

4. Results

In accordance with the solar cycle, there is only one event during solar minimum in 2007 and 2008, with more occurring in 2009 and most of the events occurring in 2010 – 2015. The yearly event count, plotted with the sunspot number and the CME rate, is shown in Figure 1. The overall CME rate is determined by the Solar Eruptive Event Detection System (SEEDS), an automatic CME detection algorithm developed at George Mason University[3] (Olmedo *et al.*, 2008).

The average characteristics of the events, broken down by flare association, are presented in Table 2. As expected, the fastest speeds as reported in the CDAW list are associated with the nine X-class flare events. This also corresponds to the events that reach Earth the fastest, although they do not have the largest *in situ* speeds. As a result of the drag force, the faster a CME is initially, the more rapidly it will decline in speed. Most of the deceleration will occur well within 1 AU and the CME speed will be largely determined by the upstream solar wind

[3] http://spaceweather.gmu.edu/seeds.

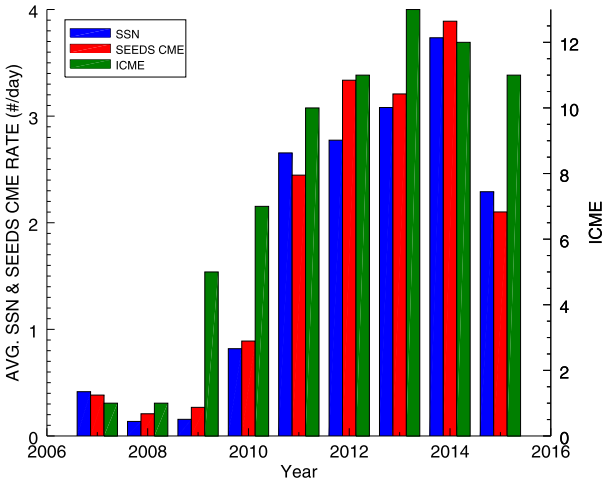

Figure 1 The levels of solar activity based on different phenomena in Cycle 24, plotted by year. The average daily SSN *per* year (blue; WDC-SILSO, Royal Observatory of Belgium, Brussels), the average daily CME rate *per* year, based on SEEDS detections (red), and the number of ICME events from the list (green).

Table 2 The properties of the events broken down by flare strength. The speeds given are all in km s^{-1}. The transit time (TT) is given in hours, based on the first appearance of the CME in LASCO and arrival *in situ*. The *in situ* speed is the average speed of the event during the *in situ* passing period based on ACE observations, the transit speeds is based on the transit time from the Sun to the Earth. The CDAW speeds are the average linear speed reported in the catalog, and the widths are given in degrees. The *in situ* magnetic field strength ($|B|$) is given in nT based on ACE data.

	Events	Shocks	TT	*In situ* speed	Transit speed	CDAW speed	CDAW width	$\|B\|$	QR
All events	70	45	80	400	500	655	258	10.6	2.13
No flare	29	15	93	394	423	419	206	10.3	2.21
B	4	2	87	480	508	376	176	8.5	1.50
C	9	7	84	409	468	612	284	10.8	1.78
M	20	17	63	461	582	904	317	11.2	2.15
X	8	4	69	426	605	1072	312	10.7	2.5

speed by the time it reaches Earth (Cargill, 2004; Poomvises, Zhang, and Olmedo, 2010; Subramanian, Lara, and Borgazzi, 2012; Vršnak *et al.*, 2013; Hess and Zhang, 2015).

The ICME events corresponding to C, M, and X class flares on the Sun all have similar magnetic field strengths *in situ*. The few events associated with B-class flares show extremely weak CDAW speeds and magnetic field strengths. The events that are associated with quiet-Sun filament eruptions have a magnetic field strength between these two classifications and also have slower coronagraph speeds. The flare events are slightly more likely to drive shocks that can be seen *in situ* than the quiet-Sun eruptions, which is most likely due to the slower initial speeds.

Surprisingly, as the flare strength increases, the quality rating of the event decreases. The probable cause of this is the more limited spatial extent of weaker CMEs. Many of the events associated with stronger flares have source regions farther from the Sun–Earth line, but because they drive powerful shocks and have strong internal magnetic fields that lead to increased expansion, they are able to strike Earth away from the CME nose where the

Table 3 The properties of the events, broken down by geoeffectiveness. The speeds are all in $\mathrm{km\,s^{-1}}$. The transit time (TT) is given in hours, based on the first appearance of the CME in LASCO and arrival *in situ*. The *in situ* speed is the average speed of the event based on ACE observations, and the transit speed is based on transit time. The CDAW speeds are the average linear speed reported in the catalog, and the widths are given in degrees. The *in situ* magnetic field strength ($|B|$) is given in nT and is based on ACE data.

	Events	Shocks	TT	*In situ* speed	Transit speed	CDAW speed	CDAW width	$\lvert B\rvert$	QR
All events	70	45	80	400	500	655	258	10.6	2.13
Dst > -40 nT	23	11	90	392	461	549	226	8.3	2.30
-100 nT $<$ Dst < -40 nT	35	21	82	427	492	631	256	10.6	2.09
Dst < -100 nT	12	12	58	460	599	965	331	13.3	1.92

Table 4 The properties of the events, broken down by projected angular width of the CMEs. The speeds are all in $\mathrm{km\,s^{-1}}$. The transit time (TT) is given in hours, based on the first appearance of the CME in LASCO and arrival *in situ*. The *in situ* speed is the average speed of the event based on ACE observations, the transit speed is based on transit time. The CDAW speeds are the average linear speed reported in the catalog, and the widths are given in degrees. The *in situ* magnetic field strength ($|B|$) is given in nT and is based on ACE data.

	Events	Shocks	TT	*In situ* speed	Transit speed	CDAW speed	$\lvert B\rvert$	QR
All events	70	45	80	400	500	654	10.6	2.13
Full halos	34	30	68	416	555	899	10.8	2.06
Partial halos	20	11	89	388	452	454	10.5	2.25
Not halo	11	1	103	363	424	265	8.9	2.18

strong, classic magnetic cloud signatures are more likely to be observed. For the smaller, weaker events, they will either strike Earth near the CME nose or will miss it entirely.

The same statistics are presented in Table 3, broken down instead by Dst index. Because the *in situ* measurements are taken close to Earth, the correlation between *in situ* signatures and Dst index is often quite strong. As would be expected, the strong geomagnetic storms (Dst < -100 nT) correspond to the fastest *in situ* speeds, transit speeds, and by far the fastest CDAW speeds. These events also clearly possess the strongest magnetic fields and on average are the events that are most clearly associated with ICMEs. The average quality rating would likely be even lower if it were not for the high correlation between geomagnetic activity and complex, multiple interacting structures. All 12 of these events in Cycle 24 appear to drive shocks at Earth as well, which makes sense since they are the strongest events in the sample.

The events can be further broken down by projected angular width in coronagraphs, as determined by CDAW, in Table 4. Halo CMEs, which present a signature at all position angles around the Sun, are generally associated with CMEs that originate near disk center and propagate toward an observer. Even before STEREO, the association between full halos and geoeffectiveness was well understood (Webb *et al.*, 2000). Halos and partial halos, where a CME front has an apparent width between 120° and 360°, especially those propagating farther away from the observer, are also indicative of the presence of a shock front (Kwon, Zhang, and Vourlidas, 2015).

Nearly half the events in the list are full halos, and these events are also the fastest events both near the Sun and at 1 AU. Thirty of the 34 full halo events have well observed *in*

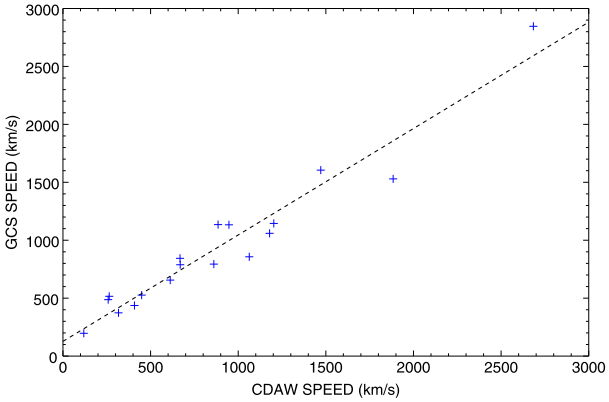

Figure 2 The relationship between the CDAW-measured velocity of the events and the speed determined by the GCS fitting.

situ shocks and also the strongest *in situ* magnetic fields. Similarly, the 11 events that were not registered as even partial halos are noticeably slower and weaker than the other events, indicative of a weaker impact along the flank of the flux rope. Of the ten events in with Dst peak < -100 nT that were also included in the CDAW catalog, eight are full halos and the other two are partial halos.

In addition to having just the CDAW velocities, which are linear fits to height measurements in LASCO coronagraphs, we have also fit a number of the events in this sample with the GCS model to determine the true deprojected speed based on a three-dimensional geometry. The GCS fittings, taking advantage of the multiple viewpoints, should be more accurate than the LASCO height measurements. Figure 2 shows the relationship between the CDAW speeds, based on a linear fit to height time measurements, and the GCS speeds, based on a linear fit to the measurements in a roughly comparable field of view. The CDAW measurements are determined by approximating a radial height at a selected position angle (Yashiro *et al.*, 2004). On average, the two show a good agreement, with an r^2 of 0.94. The GCS values are consistently higher, causing the y-intercept of the line of best fit to be 127.0 km s^{-1}. This is probably because the events we chose to measure are halo CMEs, and these velocities tend to be underestimated when using a plane-of-sky speed from one observer (Vršnak *et al.*, 2007; Howard, Nandy, and Koepke, 2008; Gopalswamy *et al.*, 2010; Jang *et al.*, 2016). In a larger sample of events from a similar time frame, Shen *et al.* (2013) also found a trend where the GCS velocity is more likely to be higher than the CDAW velocity, with a larger difference as events become faster, which matches the behavior seen in Figure 2.

4.1. CME Source Regions

To further visualize the data, Figures 3 and 4 show the source locations of the ICMEs, colored by quality rating. The size of the circles in each figure is determined by flare strength and Dst index, respectively.

One conclusion from these maps is that while QR1 events can be associated with a wide range of flare strengths and Dst enhancements, these events do tend to be more strongly clustered near the Sun–Earth line. All of these events having a clear *in situ* signature are within 45° in latitude from the equator and 36° in longitude from the central meridian. Nine of the 12 events are within 20° in longitude from the central meridian, indicating that it is important for an event to be close in longitude to the disk center to produce a clear signal *in situ*.

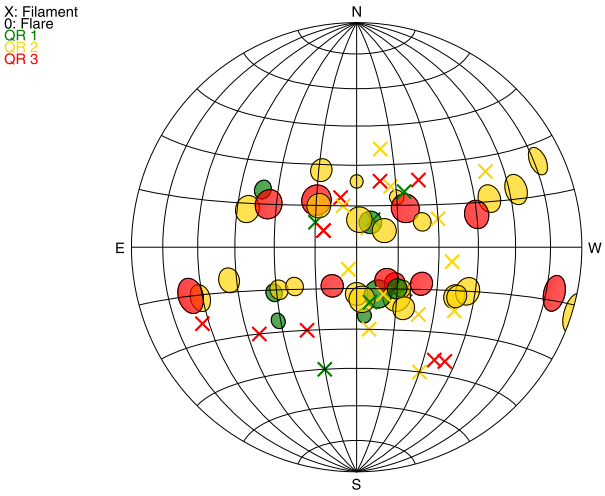

Figure 3 A map of the source regions of the CMEs that are observed by ACE. The color-coding is given by the quality rating (green = 1, yellow = 2, red = 3). Quiet-Sun eruptions are marked with an X, while CMEs associated with flares are marked with a circle; the circle size corrresponds to the flare strength. The solar disk map is a Lambert azimuthal projection.

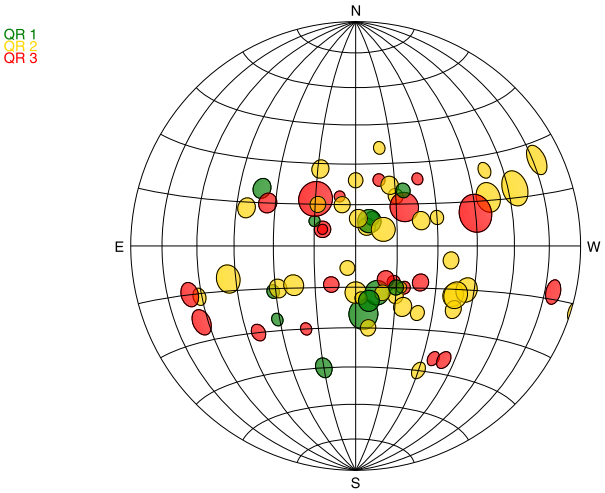

Figure 4 A map of the source regions of the CMEs that are observed by ACE. The color-coding is given by the quality rating (green = 1, yellow = 2, red = 3). The size of the circles corresponds to the observed Dst index associated with the event, with larger circles corresponding to larger geomagnetic disturbances. The solar disk map is a Lambert azimuthal projection.

Figure 3 shows a wide variety of flare or filament associations near disk center, but closer to the limb, nearly all the events are associated with larger flares. For an event close to the limb to have any kind of noticeable impact near the Earth, it has to be large in size and/or drive a strong shock. For such an event to be strong enough to be detected so far away from its initial eruption direction, it will be more likely associated with a powerful flare. The source longitude that corresponds to a B-class flare is in average of 12.3° from the central meridian, while for C-, M-, and X-class flares this increases to 25.2°, 28.7°, and 40.5°, respectively.

The geoeffective events that are classic magnetic clouds (*i.e.* quality rating of 1) come from closer to disk center, as seen in Figure 4. There are events closer to the limb whose interplanetary B_z component in geocentric solar ecliptic coordinates (GSC) is strong enough to drive a geomagnetic storm, but there will be a higher likelihood of encountering the necessary magnetic field strength to drive geomagnetic activity in a flux rope if the CME encounters Earth close to the nose. However, for events farther from the center of the disk

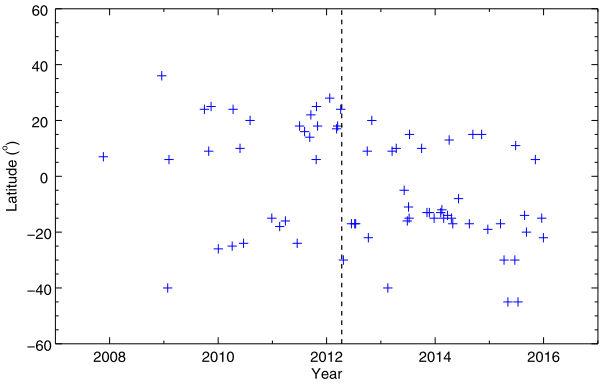

Figure 5 The latitude of the detected events, plotted with time. Before the vertical dashed line (April 2012), 71.4% of events come from the northern hemisphere. After this point, 73.8% of the events come from the southern hemisphere.

that drive geomagnetic activity, including some of the most powerful Dst events of Solar Cycle 24, the *in situ* signatures are more complex. These signatures are more commonly associated with events that on their own would not have been expected to be particularly geoeffective, but that drove an intense storm as a result of interactions with another transient structure.

Zhang *et al.* (2007) examined the source location of all geomagnetic storms with a Dst lower than −100 nT between 1996 and 2005. The most striking difference between this present study and that previous work is the large difference in the number of these events far in Cycle 24. In the ten-year period examined by Zhang *et al.* (2007), 65 CMEs that generated an intense geomagnetic storm were observed. In our sample between 2007 and 2015, only 12 such events were identified.

Zhang *et al.* (2007) showed that of the 65 events, 56 were within 45° in longitude of the central meridian (86%). Forty-nine events (75%) were within 30° and 34 (52%) were within 15°. The average longitude of the events was 12°W. In our much smaller sample of 12 of such events in Cycle 24, we find evidence that these extremely geoeffective events are more spatially spread out, as 10 events (83%) are within 45°, but just 7 (58%) are within 30° and 4 (33%) are within 15°. The average longitude of the Cycle 24 events is 18°W. This may not be a significant difference as just one or two additional events in our limited sample could drastically alter the results.

Figure 5 shows the latitude of the source regions of the ICME events as a function of time. In the period before April 2012, 20 of the 28 (71.4%) events originate in the northern hemisphere. After April 2012, this trend reverses and just 11 of 42 events (26.2%) have source locations in the northern hemisphere. This matches observations of sunspot number and magnetic field strength, which show increased activity in the northern hemisphere in the beginning of Cycle 24, later this switches and the southern hemisphere becomes more active (Karna, Pesnell, and Zhang, 2015). The source regions seem to generally follow the butterfly diagram, which shows the trend of active-region formation to progress to the equator as the solar cycle progresses (Hathaway, 2010). The CME activity in each hemisphere will generally follow this active region belt in each hemisphere (Gopalswamy *et al.*, 2003).

As expected, there does not seem to be a clear trend in the longitude of the events with time. Unlike latitude, there is no evidence that CME activity would be more likely at any particular range of longitudes. In the longitude, only a slight majority of events are observed to come from the west, as 44 of 70 (63%) erupted from the western hemisphere. This bias of events to come from the west matches a study of events from Cycle 23 by Richardson and Cane (2010), as well as other studies of CME source locations (Zhao and Webb, 2003;

Zhang *et al.*, 2007; Wang *et al.*, 2011; Lee *et al.*, 2014), which found that 57% of the events come from the western hemisphere. The western hemisphere was also source of four of the five CMEs from beyond 70° away from the Sun–Earth line. Physically, this can most likely be attributed to the Parker spiral of the solar wind. A CME propagating radially and faster than the solar wind, as most of our events are, will be deflected to the east by the solar wind (Wang *et al.*, 2004, 2006, 2014).

4.2. Comparison with Other Studies

Richardson and Cane (2010) presented a comprehensive ICME list for Cycle 23, finding 322 probable events between 1996 and 2009. This list and the list of events we have presented for Cycle 24 overlap between 2007 and 2009. The Richardson and Cane (2010) list seems to be more inclusive, as it contains 15 events during this time, while our list contains just 7. All but one of the events on our list between 2007 and 2009 are also included in Richardson and Cane (2010), so it seems that there are just more events in that study. This may be in part because of the ability we have had to remove events that present no clear white-light CME in SECCHI data for the period when these data are available. As Richardson and Cane (2010) note, nearly half of their events present no identifiable solar signature. The list has been updated since publication and can be accessed online.[4]

The additional events of Richardson and Cane (2010) may make a direct comparison difficult. The Richardson and Cane (2010) list shows CMEs with an average *in situ* velocity of 474 km s^{-1}, with an average magnetic field strength of 10.1 nT, and an average size of 0.33 AU. Removing the events from our sample that we consider to be only shocks without an associated CME signature behind them, our observed CME ejecta have an average velocity of 400 km s^{-1} and an average magnetic field strength of 10.5 nT. The average size of the events is 0.31 AU. This also compares to the size of events for intense events in Cycle 23 (Zhang, Poomvises, and Richardson, 2008).

The average parameters for all of our events can be compared to the other ICME studies that have been performed on Cycle 24. Gopalswamy *et al.* (2015) presents 65 magnetic clouds in Cycle 24, with an average velocity of 402 km s^{-1} and an average magnetic field strength of 12.3 nT. However, these events have an average duration of 19.2 hours and an average size of 0.17 AU, while the events in our sample have averages of more than 31 hours and 0.31 AU. This reveals a significant difference between the two studies in the selection of the CME boundaries that may make any direct comparison pointless, despite the agreement in average velocity. This is probably also the reason why our list has weaker magnetic fields, as we are including more material farther away from the flux rope core within our selected boundaries.

Wu and Lepping (2016), using observations from the *Wind* spacecraft, found 168 magnetic cloud events in an 18-year span and 197 magnetic-cloud-like events with an average of 9.3 magnetic clouds and 20.3 total events *per* year from *Wind*. Our list includes an average of 8.9 events *per* year, which indicates that a better comparison may be found by focusing on just the magnetic clouds from Wu and Lepping (2016) and excluding the magnetic-cloud-like events. The included set has an average velocity of 440 km s^{-1} and 12.3 nT. With average magnetic cloud time durations of 18.8 hours, it is again difficult to determine if the difference between the lists is the sample of events selected, or the selection of the boundaries on common events.

[4] http://www.srl.caltech.edu/ACE/ASC/DATA/level3/icmetable2.htm.

Wu and Lepping (2016) also break events down by whether a magnetic cloud is associated with a shock, with similar results as we have presented in Table 3. Each study shows that a shock associated event will be far more likely to lead to a strong geomagnetic storm. 60.1% of the events in our sample show shocks, while Wu and Lepping (2016) show 55.9% of all events to contain shocks.

Chi *et al.* (2016) created a comprehensive catalog using ACE and *Wind* observations from 1995 – 2015. This catalog, focused on *in situ* signatures, shows strong overlap with Richardson and Cane (2010). The events in the Chi *et al.* (2016) have an average magnetic field strength of 10.08 nT and an average velocity of 433 $\mathrm{km\,s^{-1}}$. The shock-associated events in the Chi *et al.* (2016) list have an average sheath magnetic field of 12.94 nT, much higher than the 10.74 nT sheath in our sample.

Like Wu and Lepping (2016), Chi *et al.* (2016) also divided all events into magnetic clouds and non-magnetic clouds. In that study, 61% of the magnetic clouds drove shocks and just 43% of non-magnetic clouds drove shocks. The higher percentage of shock-driving events in our list is comparable to the percentage of shocks associated with magnetic clouds in other studies. This reinforces our assumption that the selection criteria placed on events in our catalog makes it more likely that our events are associated with the events that are classified as magnetic clouds in previous studies. There is also an added level of difficulty in comparing our list to the Wu and Lepping (2016) and Chi *et al.* (2016) lists, of course, given the extended time period of these studies in comparison to ours.

Another catalog, based entirely on *Wind* observations, has also been compiled on the satellite website.[5] This catalog spans from 1995 through November of 2015. Like many of the other catalogs we discussed, this list appears more inclusive than ours and has many more events than our list. There are 14 events from our list that are missing from the *Wind* catalog, nine of them are QR3 events that are more ambiguous. Of the five QR2 events that are missing from this catalog, many possess signs of a possible interaction between multiple transients (such as the 17 March 2015 ICME, which caused a severe geomagnetic storm and is almost certainly CME related). Therefore this may only be a difference in terms of the specific structures that the two different studies are focused on. There was a single QR1 event (from July 2015) that did not appear in the *Wind* catalog.

5. Conclusions

We have identified 70 ICMEs using ACE data. Each event has been associated with a white-light CME observation in SECCHI data and was followed backwards to the Sun. This comprehensive Sun-to-Earth study of CME-ICME events was not possible before the launch of the STEREO spacecraft in 2006, but has left a unique opportunity in Solar Cycle 24. By taking the time to verify the coronal structure that is later seen *in situ*, we can verify the conditions near the Sun that cause geomagnetic activity at Earth.

We find that as expected, the flare strength is well correlated with initial speed and magnetic field strength for the CME. We can also confirm that CME speed and magnetic field are well correlated with geomagnetic activity. ICME activity is clearly dependent on the solar cycle, in terms of both frequency and magnitude of events. Additionally, as CME source regions follow the general trend of solar activity to shift toward the equator as the solar cycle progresses, we also see an asymmetry between the frequency of events in the northern and

[5] https://wind.nasa.gov/fullcatalogue.php.

southern hemisphere in Cycle 24 that mirrors observed trends in magnetic field differences in each hemisphere.

There is a significant amount of ambiguity in determining whether a signature observed *in situ* is an ICME. Relating these signatures to observed white-light CMEs can prevent any false events from entering our event sample. This still leaves a subjective element in terms of the boundaries of each event. The sizes of our events are much larger than in other studies of ICMEs in Cycle 24 (Gopalswamy *et al.*, 2015; Wu and Lepping, 2016), but comparable to a study of events in Cycle 23 (Richardson and Cane, 2010).

The improved ability to track these events from the Sun to the Earth demonstrates the usefulness of SECCHI data and can improve the physical understanding of CME propagation. Having a complete dataset that overlaps and includes the initial eruption, propagation, and *in situ* arrival of the CME is a unique observational benefit for studying CME events in Cycle 24.

Acknowledgements We thank the anonymous referee for useful suggestions that improved the quality of this manuscript. This research was performed while Phillip Hess held an NRC Research Associateship award at the U.S. Naval Research Laboratory. JZ is supported by NSF AGS-1249270 and AGS-1460188. The SECCHI data are produced by an international consortium of NRL, LMSAL, and NASA GSFC (USA), RAL and U. Bham (UK), MPS (Germany), CSL (Belgium), IOTA and IAS (France). The SOHO/LASCO data used here are produced by a consortium of the Naval Research Laboratory (USA), Max-Planck-Institut fuer Sonnensystemforschung (Germany), Laboratoire d'Astronomie (France), and the University of Birmingham (UK). SOHO is a project of international cooperation between ESA and NASA. The AIA data are courtesy of SDO (NASA) and the AIA consortium. The SSN used was obtained from the WDC-SILSO, Royal Observatory of Belgium, Brussels. Active region and flare information was obtained from NOAA.

Disclosure of Potential Conflicts of Interest The authors declare that they have no conflicts of interest.

References

Brueckner, G.E., Howard, R.A., Koomen, M.J., Korendyke, C.M., Michels, D.J., Moses, J.D., Socker, D.G., Dere, K.P., Lamy, P.L., Llebaria, A., Bout, M.V., Schwenn, R., Simnett, G.M., Bedford, D.K., Eyles, C.J.: 1995, The Large Angle Spectroscopic Coronagraph (LASCO). *Solar Phys.* **162**, 357. DOI.

Burlaga, L.F.: 1988, Magnetic clouds and force-free field with constant alpha. *J. Geophys. Res.* **93**, 7217. DOI.

Burlaga, L.F., Plunkett, S.P., St. Cyr, O.C.: 2002, Successive CMEs and complex ejecta. *J. Geophys. Res.* **107**, 1266. DOI.

Cargill, P.J.: 2004, On the aerodynamic drag force acting on interplanetary coronal mass ejections. *Solar Phys.* **221**, 135. DOI. ADS.

Chi, Y., Shen, C., Wang, Y., Xu, M., Ye, P., Wang, S.: 2016, Statistical study of the interplanetary coronal mass ejections from 1995 to 2015. *Solar Phys.* **291**, 2419. DOI. ADS.

Delaboudinière, J.-P., Artzner, G.E., Brunaud, J., Gabriel, A.H., Hochedez, J.F., Millier, F. *et al.*: 1995, EIT: Extreme-Ultraviolet Imaging Telescope for the SOHO mission. *Solar Phys.* **162**, 291. DOI.

Gopalswamy, N., Lara, A., Kaiser, M.L., Bougeret, J.-L.: 2001, Near-Sun and near-Earth manifestations of solar eruptions. *J. Geophys. Res.* **106**, 25261. DOI.

Gopalswamy, N., Lara, A., Yashiro, S., Howard, R.A.: 2003, Coronal mass ejections and solar polarity reversal. *Astrophys. J. Lett.* **598**, L63. DOI. ADS.

Gopalswamy, N., Yashiro, S., Michalek, G., Xie, H., Mäkelä, P., Vourlidas, A., Howard, R.A.: 2010, A catalog of halo coronal mass ejections from SOHO. *Sun Geosph.* **5**, 7. ADS.

Gopalswamy, N., Yashiro, S., Xie, H., Akiyama, S., Mäkelä, P.: 2015, Properties and geoeffectiveness of magnetic clouds during Solar Cycles 23 and 24. *J. Geophys. Res.* **120**, 9221. DOI.

Hathaway, D.H.: 2010, The solar cycle. *Living Rev. Solar Phys.* **7**, 1. DOI. ADS.

Hess, P., Zhang, J.: 2014, Stereoscopic study of the kinematic evolution of a coronal mass ejection and its driven shock from the Sun to the Earth and the prediction of their arrival times. *Astrophys. J.* **792**, 49. DOI. ADS.

Hess, P., Zhang, J.: 2015, Predicting CME ejecta and sheath front arrival at L1 with a data-constrained physical model. *Astrophys. J.* **812**(2), 144. DOI.

Howard, R.A., Moses, J.D., Vourlidas, A., Newmark, J.S., Socker, D.G., Plunkett, S.P., Korendyke, C.M., Cook, J.W., Hurley, A., Davila, J.M., Thompson, W.T., St. Cyr, O.C., Mentzell, E., Mehalick, K., Lemen, J.R., Wuelser, J.P., Duncan, D.W., Tarbell, T.D., Wolfson, C.J., Moore, A., Harrison, R.A., Waltham, N.R., Lang, J., Davis, C.J., Eyles, C.J., Mapson-Menard, H., Simnett, G.M., Halain, J.P., Defise, J.M., Mazy, E., Rochus, P., Mercier, R., Ravet, M.F., Delmotte, F., Auchere, F., Delaboudiniere, J.P., Bothmer, V., Deutsch, W., Wang, D., Rich, N., Cooper, S., Stephens, V., Maahs, G., Baugh, R., McMullin, D., Carter, T.: 2008, Sun Earth Connection Coronal and Heliospheric Investigation (SECCHI). *Space Sci. Rev.* **136**, 67. DOI. ADS.

Howard, T.A., Nandy, D., Koepke, A.C.: 2008, Kinematic properties of solar coronal mass ejections: Correction for projection effects in spacecraft coronagraph measurements. *J. Geophys. Res.* **113**, A01104. DOI. ADS.

Jackson, B.V.: 1986, HELIOS photometer measurement of *in situ* density enhancements. *Adv. Space Res.* **6**, 307. DOI. ADS.

Jang, S., Moon, Y.-J., Kim, R.-S., Lee, H., Cho, K.-S.: 2016, Comparison between 2D and 3D parameters of 306 front-side halo CMEs from 2009 to 2013. *Astrophys. J.* **821**, 95. DOI. ADS.

Karna, N., Pesnell, W.D., Zhang, J.: 2015, Appearances and statistics of coronal cavities during the ascending phase of Solar Cycle 24. *Astrophys. J.* **810**(2), 123. DOI.

Kwon, R.-Y., Zhang, J., Vourlidas, A.: 2015, Are halo-like solar coronal mass ejections merely a matter of geometric projection effects? *Astrophys. J. Lett.* **799**, L29. DOI. ADS.

Lee, J.-O., Moon, Y.-J., Lee, K.-S., Kim, R.-S.: 2014, dependence of geomagnetic storms on their associated halo CME parameters. *Solar Phys.* **289**, 2233. DOI. ADS.

Lemen, J., Title, A., Akin, D., Boerner, P., Chou, C., Drake, J., Duncan, D., Edwards, C., Friedlaender, F., Heyman, G., Hurlburt, N., Katz, N., Kushner, G., Levay, M., Lindgren, R., Mathur, D., McFeaters, E., Mitchell, S., Rehse, R., Schrijver, C., Springer, L., Stern, R., Tarbell, T., Wuelser, J.-P., Wolfson, C.J., Yanari, C., Bookbinder, J., Cheimets, P., Caldwell, D., Deluca, E., Gates, R., Golub, L., Park, S., Podgorski, W., Bush, R., Scherrer, P., Gummin, M., Smith, P., Auker, G., Jerram, P., Pool, P., Soufli, R., Windt, D., Beardsley, S., Clapp, M., Lang, J., Waltham, N.: 2012, The Atmospheric Imaging Assembly (AIA) on the Solar Dynamics Observatory (SDO). *Solar Phys.* **275**, 17. DOI.

Lugaz, N., Farrugia, C.J., Huang, C.-L., Spence, H.E.: 2015, Extreme geomagnetic disturbances due to shocks within CMEs. *Geophys. Res. Lett.* **42**, 4694. DOI. ADS.

Möstl, C., Farrugia, C.J., Kilpua, E.K.J., Jian, L.K., Liu, Y., Eastwood, J.P., Harrison, R.A., Webb, D.F., Temmer, M., Odstrcil, D., Davies, J.A., Rollett, T., Luhmann, J.G., Nitta, N., Mulligan, T., Jensen, E.A., Forsyth, R., Lavraud, B., de Koning, C.A., Veronig, A.M., Galvin, A.B., Zhang, T.L., Anderson, B.J.: 2012, Multi-point shock and flux rope analysis of multiple interplanetary coronal mass ejections around 2010 August 1 in the inner heliosphere. *Astrophys. J.* **758**, 10. DOI. ADS.

Olmedo, O., Zhang, J., Wechsler, H., Poland, A., Borne, K.: 2008, Automatic detection and tracking of coronal mass ejections in coronagraph time series. *Solar Phys.* **248**, 485. DOI. ADS.

Poomvises, W., Zhang, J., Olmedo, O.: 2010, Coronal mass ejection propagation and expansion in three-dimensional space in the heliosphere based on Stereo/SECCHI observations. *Astrophys. J. Lett.* **717**, L159. DOI. ADS.

Pulkkinen, T.: 2007, Space weather: Terrestrial perspective. *Living Rev. Solar Phys.* **4**, 1. DOI. ADS.

Richardson, I.G., Cane, H.V.: 1995, Regions of abnormally low proton temperature in the solar wind (1965 – 1991) and their association with ejecta. *J. Geophys. Res.* **100**, 23397. DOI.

Richardson, I.G., Cane, H.V.: 2004, Identification of interplanetary coronal mass ejections at 1 AU using multiple solar wind plasma composition anomalies. *J. Geophys. Res.* **109**, 9104. DOI.

Richardson, I.G., Cane, H.V.: 2010, Near-Earth interplanetary coronal mass ejections during Solar Cycle 23 (1996 – 2009): Catalog and summary of properties. *Solar Phys.* **264**, 189. DOI. ADS.

Richardson, I.G., Webb, D.F., Zhang, J., Berdichevsky, D.B., Biesecker, D.A., Kasper, J.C., Kataoka, R., Steinberg, J.T., Thompson, B.J., Wu, C.-C., Zhukov, A.N.: 2006, Major geomagnetic storms ($Dst \leq -100$ nT) generated by corotating interaction regions. *J. Geophys. Res.* **111**(A10), 7. DOI.

Rouillard, A.P.: 2011, Relating white light and *in situ* observations of coronal mass ejections: A review. *J. Atmos. Solar-Terr. Phys.* **73**, 1201. DOI. ADS.

Shen, C., Wang, Y., Pan, Z., Zhang, M., Ye, P., Wang, S.: 2013, Full halo coronal mass ejections: Do we need to correct the projection effect in terms of velocity? *J. Geophys. Res. (Space Physics)* **118**, 6858. DOI. ADS.

Shen, C., Wang, Y., Pan, Z., Miao, B., Ye, P., Wang, S.: 2014, Full-halo coronal mass ejections: Arrival at the Earth. *J. Geophys. Res.* **119**, 5107. DOI.

Stone, R.G., Frandsen, A.M., Mewaldt, R.A., Christian, E.R., Margolies, D., Ormes, J.F., Snow, F.: 1998, The advanced composition explorer. *Space Sci. Rev.* **86**, 1. DOI.

Subramanian, P., Lara, A., Borgazzi, A.: 2012, Can solar wind viscous drag account for coronal mass ejection deceleration? *Geophys. Res. Lett.* **39**, 19107. DOI. ADS.

Temmer, M., Nitta, N.V.: 2015, Interplanetary propagation behavior of the fast coronal mass ejection on 23 July 2012. *Solar Phys.* **290**, 919. DOI. ADS.

Thernisien, A.F.R., Howard, R.A., Vourlidas, A.: 2006, Modeling of flux rope coronal mass ejections. *Astrophys. J.* **652**, 763. DOI. ADS.

Vršnak, B., Sudar, D., Ruždjak, D., Žic, T.: 2007, Projection effects in coronal mass ejections. *Astron. Astrophys.* **469**, 339. DOI. ADS.

Vršnak, B., Žic, T., Vrbanec, D., Temmer, M., Rollett, T., Möstl, C., Veronig, A., Čalogović, J., Dumbović, M., Lulić, S., Moon, Y.-J., Shanmugaraju, A.: 2013, Propagation of interplanetary coronal mass ejections: The drag-based model. *Solar Phys.* **285**, 295. DOI. ADS.

Wang, Y.M., Ye, P.Z., Wang, S.: 2003, Multiple magnetic clouds: Several examples during March–April, 2001. *J. Geophys. Res.* **108**, 1370. DOI.

Wang, Y.M., Ye, P.Z., Wang, S., Zhou, G.P., Wang, J.X.: 2002, A statistical study on the geoeffectiveness of earth-directed coronal mass ejections from March 1997 to December 2000. *J. Geophys. Res.* **107**, 1340. DOI.

Wang, Y.M., Ye, P.Z., Wang, S., Xue, X.H.: 2003a, An interplanetary cause of large geomagnetic storms: Fast forward shock overtaking preceding magnetic cloud. *Geophys. Res. Lett.* **30**(13), 1700. DOI.

Wang, Y.M., Ye, P.Z., Wang, S., Xiong, M.: 2003b, Theoretical analysis on the geoeffectiveness of shock overtaking preceding magnetic cloud. *Solar Phys.* **216**, 295. DOI.

Wang, Y., Shen, C., Ye, P., Wang, S.: 2004, Deflection of coronal mass ejection in the interplanetary medium. *Solar Phys.* **222**, 329. DOI.

Wang, Y., Zhou, G., Ye, P., Wang, S., Wang, J.: 2006, A study of the orientation of interplanetary magnetic clouds and solar filaments. *Astrophys. J.* **651**, 1245. DOI. ADS.

Wang, Y., Chen, C., Gui, B., Shen, C., Ye, P., Wang, S.: 2011, Statistical study of coronal mass ejection source locations: Understanding CMEs viewed in coronagraphs. *J. Geophys. Res.* **116**, A04104. DOI. ADS.

Wang, Y., Wang, B., Shen, C., Shen, F., Lugaz, N.: 2014, Deflected propagation of a coronal mass ejection from the corona to interplanetary space. *J. Geophys. Res.* **119**, 5117. DOI. ADS.

Webb, D.F., Cliver, E.W., Crooker, N.U., St. Cyr, O.C., Thompson, B.J.: 2000, Relationship of halo coronal mass ejections, magnetic clouds, and magnetic storms. *J. Geophys. Res.* **105**, 7491. DOI.

Wu, C.-C., Lepping, R.P.: 2016, Relationships among geomagnetic storms, interplanetary shocks, magnetic clouds, and sunspot number during 1995 – 2012. *Solar Phys.* **291**, 265. DOI. ADS.

Yashiro, S., Gopalswamy, N., Michalek, G., St. Cyr, O.C., Plunkett, S.P., Rich, N.B., Howard, R.A.: 2004, A catalog of white light coronal mass ejections observed by the SOHO spacecraft. *J. Geophys. Res.* **109**, 7105. DOI.

Zhang, J., Hess, P., Poomvises, W.: 2013, A comparative study of coronal mass ejections with and without magnetic cloud structure near the Earth: Are all interplanetary CMEs flux ropes? *Solar Phys.* **284**, 89. DOI. ADS.

Zhang, J., Poomvises, W., Richardson, I.G.: 2008, Sizes and relative geoeffectiveness of interplanetary coronal mass ejections and the preceding shock sheaths during intense storms in 1996 – 2005. *Geophys. Res. Lett.* **35**, 2109. DOI. ADS.

Zhang, J., Dere, K.P., Howard, R.A., Bothmer, V.: 2003, Identification of solar sources of major geomagnetic storms between 1996 and 2000. *Astrophys. J.* **582**, 520. DOI.

Zhang, J., Richardson, I.G., Webb, D.F., Gopalswamy, N., Huttunen, E., Kasper, J.C., Nitta, N.V., Poomvises, W., Thompson, B.J., Wu, C.-C., Yashiro, S., Zhukov, A.N.: 2007, Solar and interplanetary sources of major geomagnetic storms ($Dst \leq -100$ nT) during 1996 – 2005. *J. Geophys. Res.* **112**, 10102. DOI.

Zhao, X.P., Webb, D.F.: 2003, Source regions and storm effectiveness of frontside full halo coronal mass ejections. *J. Geophys. Res.* **108**, 1234. DOI.